

Microstructures and mechanical properties of CoCrFeMnNiV_x high entropy alloy films

Shuang Fang ^a, Cheng Wang ^{a, b}, Chia-Lin Li ^a, Jun-Hua Luan ^b, Zeng-Bao Jiao ^c, Chain-Tsuan Liu ^b, Chun-Hway Hsueh ^{a, *}

^a Department of Materials Science and Engineering, National Taiwan University, Taipei, 10617, Taiwan

^b Department of Materials Science and Engineering, City University of Hong Kong, Hong Kong, China

^c Department of Mechanical Engineering, The Hong Kong Polytechnic University, Hong Kong, China

ABSTRACT

In the present work, CoCrFeMnNiV_x (x = 0, 0.07, 0.3, 0.7, 1.1) high entropy alloy films were fabricated by magnetron co-sputtering. For low contents of V, typical face-centered cubic (fcc) peaks were identified in X-ray diffraction patterns. With the increasing V content, the diffraction peaks became broadened and the formation of an amorphous phase was promoted. TEM observations showed abundant nanotwins in the films with low V contents and the transition from fcc to the amorphous structure with the increasing V content. Mechanical properties of the films were studied using nanoindentation and micro-pillar compression tests. The films exhibited a high hardness ranging from 6.8 to 8.7 GPa. The serrated flow associated with shear banding showed in the stress-strain curves for films with x ≥ 0.3. When x = 0.07, the excellent yield strength of 3.79 GPa and ultimate compressive strength of 4.93 GPa were achieved with little sacrifice in ductility. The presence of nanotwins contributed to the strain hardening effect.

1. Introduction

High entropy alloys (HEAs), first proposed by Yeh et al. ^[1], have gained extensive research attentions due to their novel design in compositions. In contrast to the conventional alloys based

on one principal element, HEAs are multicomponent alloys ^[2] containing five or more principal elements with the atomic fraction of each element between 5 and 35 at.% ^[1]. The high mixing entropy of HEAs is considered to promote the formation of simple solid solution structures, e.g. face-centered cubic (fcc), body-centered cubic (bcc) or fcc + bcc ^[3-7]. Depending upon the constituent elements, HEAs could possess the versatile properties ^[8], such as high hardness ^[9,10], good ductility ^[11,12], high yield strength ^[13,14], high wear resistance ^[15,16], good oxidation resistance ^[17,18], enhanced irradiation resistance ^[19], and the potential materials for high temperature applications ^[20,21], etc. According to the previous studies, an fcc-structured HEA consisting of Co, Cr, Fe, Mn and Ni has been widely investigated for its excellent ductility and fracture toughness ^[22-25]. Interestingly, unlike most alloys that become brittle at low temperatures, CoCrFeMnNi HEA shows better strength, ductility, and toughness at 77 K than 200 K and 293 K. However, it exhibits a relatively weak hardness ^[26] and yield strength ^[27] at room temperature. Therefore, it is essential to improve its hardness and strength for its practical applications.

Various research efforts have been dedicated to modifying the microstructure of CoCrFeMnNi system for strength enhancements by adding different elements. For examples, V ^[26,28-30], Al ^[6,13,31,32], Mo ^[33], Nd ^[34], C ^[35] and Ti ^[36,37] have been added, respectively, to result in the formation of the intermetallic phases or bcc crystal structure. Particularly, V was regarded as a candidate for forming and stabilizing the intermetallic sigma phase ^[38]. An equiatomic CoCrFeNiMnV HEA was fabricated by arc melting, and the addition of V gave rise to the formation of the sigma phase with a tetragonal structure ^[26]. Meanwhile, the micro-hardness of CoCrFeNiMnV increased more than 3 times in comparison with CoCrFeMnNi, accompanied by the loss in ductility. A systematic study on CoCrFeMnNiV_x HEAs was conducted by Stepanov et al. ^[28] and they found that the alloy remained to be in a single fcc phase when the concentration of

V was lower than 4.6 at.%. For the V composition of 9.1 at.%, sigma phase precipitates were observed. With higher contents of V, the sigma phase became the matrix phase with isolated fcc particles [28]. Furthermore, CoCrFeNiMnV_{0.25} (with 4.6 at.% of V) was also proven to possess a higher strength at lower temperatures [39], making it a promising material for cryogenic applications.

In addition to the development of HEAs, high entropy alloy films (HEAFs) have also aroused extensive attentions because of their smaller sizes and better mechanical properties compared with their bulk counterparts [40-46]. The CoCrFeNi HEAF with an fcc structure exhibited a high hardness of 8.5 GPa, as compared with a hardness of 1.57 GPa for its bulk counterpart [26]. A five-component HEAF, CrCoCuFeNi [47], was confirmed to be a single fcc solid solution although it was deposited from a sputtering target with two fcc structure phases. This indicated that sputtering deposition of HEAFs tended to distribute elements more uniformly than casting of ingots. A refractory NbMoTaW HEAF [48] fabricated by magnetron co-sputtering was proven to exhibit a superior high yield strength of ~10 GPa and better ductility in contrast to its bulk counterpart. A series of Al_xCoCrFeNi HEAFs [49] possessing abundant nanotwins also exhibited a much higher hardness and strain rate sensitivity than the corresponding bulk counterpart. However, it is worth noting that excessive solute elements would deteriorate the mechanical properties of HEAFs. For example, Nb_xCoCrCuFeNi HEAFs would lead to a decrease in hardness when Nb content was higher than 15.2 at.% because of the formation of the amorphous phase whose plasticity was governed by shear banding rather than the propagation of dislocations [50,51]. Hence, a proper amount of the specific additive element is required to enhance the mechanical properties of HEAFs.

In the present study, a series of CoCrFeMnNiV_x HEAFs were processed to systematically investigate the effects of the V content on the microstructure, mechanical properties and

deformation mechanism of the resulting films. Also, the comparison between CoCrFeMnNiV_x HEAFs and their bulk counterparts was studied.

2. Materials and methods

2.1. Fabrication of CoCrFeMnNiV_x HEAFs

Cobalt, chromium, iron, manganese and nickel pure metals (>99.99 wt%) were used to fabricate the CoCrFeMnNi target and pure vanadium (>99.99 wt%) was used to fabricate the V target for sputtering. Specifically, the alloy ingot with the nominal composition of CoCrFeMnNi was fabricated by vacuum induction melting and then cast with the diameter of 100 mm. The as-cast ingot was annealed at 1200 °C for 2 h and water quenched for homogenization. The sputtering target with a diameter of 76.2 mm and thickness of 6 mm was then manufactured from the ingot by electrical discharge machining. CoCrFeMnNiV_x thin films were deposited on (100)-Si wafers by radio frequency (RF) magnetron co-sputtering. Before sputtering, the Si substrates were pre-rinsed in ultrasonic bath cleaning orderly with acetone, alcohol and deionized water for 15 min each, and the two targets were respectively pre-sputtered by argon ion bombardment for at least 5 min each to remove the impurities and oxide on the surface. All deposition procedures were conducted for 2 h at ambient temperature in the vacuum chamber with the base pressure of 2.0×10^{-7} Torr. Compositions of the films were determined by the powers applied on the two targets during sputtering. While the RF power applied on CoCrFeMnNi target was fixed at 200 W, the RF power applied on the V target was, respectively, set at 0, 20, 40, 60, and 80 W. The argon gas flow was 20 sccm (standard cubic centimeters per minute), and the rotation rate of the substrate was set at 20 r/m to homogenize the composition and thickness of the film. The working distance was 10 mm and the working pressure was 3 mTorr.

2.2. Characterization of composition and structure

The surface morphology, chemical composition and thickness of the as-deposited films were characterized by scanning electron microscopy (SEM, JEOL JSM 7800F), equipped with an energy dispersive X-ray spectrometer (EDS). The crystal structure and preferred orientation of the films were determined by a glancing- incidence (0.9°) X-ray diffraction (XRD, Rigaku TTRAX 3) using Cu K α radiation to scan from 20° to 100° with a scanning speed of $4^\circ/\text{min}$. The atom probe tomography (APT, LEAP 5000 XR) was employed to determine the distributions of elements in the as- deposited films. Transmission electron microscopy (TEM, FEI Tec- nai G2 F20) was used to study the nanostructure and crystallinity of the films. Both APT and TEM specimens were prepared by scanning electron microscope/focused ion beam (SEM/FIB, FEI Quanta 3D FEG) and a thick Pt layer was deposited over the surface of the films to avoid the ion-beam damage.

2.3. Characterization of mechanical properties

Mechanical properties of the films were determined using nanoindentation (Hysitron TI 950 TriboIndenter) and in-situ SEM micro-pillar compression tests (Hysitron PI 85 SEM PicoIndenter) at room temperature. Nanoindentation tests were performed under the load-controlled mode with a standard Berkovich tip. To avoid the substrate effect, the applied load was pre-tested to ensure the penetration depth being less than $1/10$ of the film thickness and a peak load of $5000\ \mu\text{N}$ was adopted. The micro-pillars were pre- pared by FIB technique with the height of $\sim 1.8\ \text{mm}$ and diameter of $0.7\ \mu\text{m}$. The compression tests were conducted by PicoIndenter equipped with a flat-punch diamond tip ($5\ \mu\text{m}$ in diameter) with the displacement-controlled mode of $2\ \text{nm/s}$ displacement rate. Specimens after deformation were manufactured to TEM foils by FIB to examine the cross-sections after micro-pillar compression tests.

3. Results and discussion

3.1. Composition and structure

Analyzed by EDS, the chemical compositions of as-deposited CoCrFeMnNiV_x HEAFs with different sputtering powers are listed in Table 1. The content of V increased with the power applied on the V target. For $x = 0, 0.07, 0.3, 0.7$ and 1.1 , the corresponding CoCr-FeMnNiV_x HEAFs were denoted as V0, V0.07, V0.3, V0.7 and V1.1, respectively.

The XRD patterns of CoCrFeMnNiV_x ($x = 0, 0.07, 0.3, 0.7$ and 1.1) HEAFs are shown in Fig. 1. A typical single fcc structure was detected in the V-free thin film ($x = 0$), and the structure was identical to the bulk CoCrFeMnNi^[52]. For $x = 0.07$, the intensity of the fcc peaks in the as-deposited film decreased but the fcc structure retained. This implied that a low solute concentration of V might not result in any structure change in the film. Peaks at about 44° were also observed for other as-deposited films; however, the peak broadened with the increasing V content, suggesting the possibility of a change from an fcc to an amorphous (or nano-crystalline) structure^[51]. Nevertheless, compared to the XRD spectra of CoCrFeMnNiV_x bulk counterparts^[28], no peaks of sigma phase could be identified for the films, and it could be attributed to the fast quenching during the magnetron sputtering deposition procedure^[47].

3.2. Microstructure

The microstructure of the cross-section of the CoCrFeMnNiV_x HEAFs and their corresponding selected area electron diffraction (SAED) patterns were characterized by TEM, and the results are shown in Fig. 2. Columnar grains with the average width of ~ 45 nm and abundant nanotwins were observed in the V0, V0.07 and V0.3 films (Fig. 2(a), (b) and (c)). According to the atomic peening effect^[53], the high energy atoms sputtered from the targets could be deposited

on the substrate with the formation of nanotwins. From the inset of SAED patterns in Fig. 2(a), (b) and (c), it could be identified that CoCrFeMnNiV_x HEAFs had a single-phase fcc structure for $x = 0, 0.07$ and 0.3 , and it agreed with the XRD results shown in Fig. 1. The thicknesses of nanotwins in V0, V0.07, V0.3 and V0.7 were 3.6 ± 0.7 nm, 6.5 ± 1.3 nm, 6.7 ± 2.5 nm and 16.2 ± 3.2 nm, respectively. The number density of nanotwins declined and a shallow amorphous ring appeared as the V content increased in the V0.3 and V0.7 films (Fig. 2(c) and (d)) while the fcc patterns could still be recognized in the SAED patterns. This indicated the presence of an amorphous structure embedded in the fcc matrix. When the content of V increased to 18.8 at.%, the high-resolution TEM (HRTEM) image of V1.1 (Fig. 2(e)) exhibits no lattice fringes corresponding to any crystalline phases. Moreover, fcc phases could no longer be found and instead a diffuse halo ring of the amorphous structure was obtained in the SAED pattern. The atomic size difference (δ) could be considered to explain the transition to the amorphous phase^[54], and

$$\delta = \sqrt{\frac{N}{\sum_{i=1}^N x_i} \left(1 - d_i / \frac{\sum_{j=1}^N x_j d_j}{N}\right)^2}, \quad (1)$$

where N is the number of elements in the alloy, x_i and x_j are the contents of the i th and j th elements, and d_i and d_j are the atomic diameters of the i th and j th elements, respectively. The atomic radii of Co, Cr, Fe, Mn, Ni and V are 152 p.m., 166 p.m., 156 p.m., 161 p.m. 149 p.m. and 171 p.m., respectively. Based on the compositions shown in Table 1, δ could be calculated from Eq. (1) and it increased from 0.95% for V0 to 4.9% for V1.1 as the content of V increased. The alloys with large values of δ tended to transform into the amorphous structure and this behavior was proven elsewhere^[54,55].

Further characterization of element distributions in CoCr-FeMnNiV_x HEAFs was conducted by 3D APT analysis. As displayed in Fig. 3(a), the as-deposited CoCrFeMnNi HEAF revealed uniform distributions of Co, Cr, Fe, Mn, and Ni. While TEM results illustrated the columnar

nanocrystalline grain structure (Fig. 2(a)), the APT reconstruction of each element revealed no segregation or cluster. The similar homogenous structure without any precipitate was also observed for CoCrFeMnNiV_{0.07} HEAF (Fig. 3(b)), suggesting that the addition of 1.4 at.% V did not lead to the phase transformation. This result was in agreement with the XRD (Fig. 1) and TEM (Fig. 2(b)) results.

3.3. Mechanical properties

The SEM images of the micro-pillars prepared from CoCr-FeMnNiV_x HEAFs after the compression tests are shown in Fig. 4, and the corresponding compressive engineering stress-strain curves are plotted in Fig. 5. As shown in Fig. 4(a) and (b), no apparent slip or shear banding were observed in V0 and V0.07, while slip and shear banding, which were considered to give rise to strain hardening, were observed in V0.3, V0.7 and V1.1 (Fig. 4(c), (d), and (e)). It can be seen from Fig. 5 that all specimens exhibited very high yield and fracture strengths. The CoCrFeMnNi HEAF showed a yield strength of ~2.3 GPa and ~19% fracture strain in compression. With the addition of V, V0.07 exhibited an enhanced yield strength of ~3.8 GPa with a reduced fracture strain of ~13.2%. It is worth noting that when 1.4 at.% V was added to CoCrFeMnNi HEAF, a unique work hardening yield stage was observed and the fracture strength was drastically improved from 3.65 to a maximum value among films of 4.93 GPa for V0.07. In addition, the pinning effect due to dislocation slip blocked by the solute atoms at the beginning of plastic deformation was observed in V0.07, and a higher stress was needed for dislocations to overcome the activation energy barrier. When the dislocations started to move away from the solute atoms, the loading stress dropped to a lower value and the pinning energy was released. Instead of precipitates, pinning effect in V0.07 was dominated by the solute atoms, which was proven by the APT results shown in Fig. 3. The increase of V content in HEAFs was accompanied by the loss in the

compressive fracture strain (ductility) from ~19% for V0 to ~10.5% for V1.1. However, the excessive V only affected the fracture strength slightly, and serrated flow associated with shear banding [56], which was often observed in the deformation of amorphous metallic glasses [57-59], could be identified in the V0.3, V0.7 and V1.1 curves. This was in agreement with the diffuse halo rings of the amorphous phase found in the TEM SAED patterns of V0.3, V0.7 and V1.1 (Fig. 2(c), (d) and (e)).

The measured yield strength (σ_y), fracture strength (σ_f), fracture strain (ϵ_f), hardness (H) and Young's modulus (E) of the films are listed in Table 2, where σ_y , σ_f and ϵ_f were obtained from micro-pillar compression tests with σ_y defined as the stress at which the serration was first observed while hardness and Young's modulus were obtained from nanoindentation. The Young's modulus of the sample was calculated from the equation of Young's modulus and reduced Young's modulus [60].

$$\frac{1}{E_r} = \left(\frac{1 - \nu^2}{E} \right)_{\text{sample}} + \left(\frac{1 - \nu^2}{E} \right)_{\text{indenter}} \quad (2)$$

The modulus and Poisson's ratio of the indenter were 1141 GPa and 0.07, respectively. The value of Poisson's ratio was obtained from the study elsewhere for CoCrFeMnNi HEAs (= 0.313) [61].

The hardness and Young's modulus of CoCrFeMnNiV_x HEAFs as functions of the power applied on the V target are shown in Fig. 6. With the increase of power and V content, the hardness increased from ~6.8 to ~8.7 GPa, suggesting the constituent of V has a pronounced effect on the microhardness of the films. Compared to bulk CoCrFeMnNiV_x alloy [28], the film showed a similar tendency of increasing hardness with the increasing V content. However, the films exhibited noticeably higher hardness than the bulk counterparts (1.4-6.4 GPa). It is prevalingly attributed to the ultra-fine grains and a large number of nanotwins found in the films. The mechanism of such

grain-size strengthening is commonly referred as the “Hall-Petch effect” [62-65]. Also, generating nanotwins was deemed as an effective method to strengthen alloys because the emergence of nanotwins could hinder the propagation of dislocations as well as dislocation-twin boundary interaction hardening in fine twins [66]. The 1.4 at.% V-doped V0.07 film exhibited the highest Young’s modulus and fracture strength among all which was mainly attributed to the solid solution strengthening [67]. Considering the widths of columnar grains in V0, V0.07, V0.3 and V0.7 were almost the same, the density of twins (substructure strengthening) and content of V (solid solution strengthening) dominated and optimized the mechanical properties of V0.07. Further increase in the V content resulted in the decrease in Young’s modulus because of the presence of amorphous phase in V0.3, V0.7 and V1.1. It was analogously found that the moderate addition of V in bulk AlCoCrFeNiV_{0.2} (with 3.85 at.% of V) alloy possessed better mechanical properties than other alloys in the AlCoCrFeNiV_x HEAs due to V-doped solid solution strengthening [38].

During deformation, the stability of dislocations and nanotwins have a strong impact on the mechanical properties of alloys [49,68,69]. To study the microstructural change resulting from the micro-pillar compression tests, the TEM analyses on the cross section of the deformed pillars were conducted and the images are shown in Figs. 7 and 8. The TEM image of V0 after the micro-pillar compression test is shown in Fig. 7(a) and the image with a higher magnification is shown in Fig. 8(a) with the corresponding SAED shown in the inset. Comparing Fig. 8(a) with Fig. 2(a), columnar nanocrystalline-grains of CoCrFeMnNi HEAF could be hardly observed and the fraction of nanotwins decreased dramatically after deformation. As nanotwins provide obstacles to dislocation motion, the CoCrFeMnNi HEAF exhibits not only a more superior hardness (6.77 GPa) but also yield strength (2.30 GPa) than the bulk counterpart [28]. Similar to Figs. 7(a) and 8(a) for V0, the corresponding results are shown in Figs. 7(b) and 8(b) for V0.07 and in Figs. 7(c) and 8(c)

for V0.3. Fig. 8(b) presented disordered features while previously mentioned nanotwins in Fig. 2(b) dwindled. The analogous resulting microstructure after compression was also observed in $\text{Al}_{0.1}\text{CoCrFeNi}$ HEAFs on the top of the deformed region after nanoindentation [22]. Hence, the work hardening stage in V0.07 curve in Fig. 5 was consistent with the detwinning behavior [22]. Fig. 7(c) shows a deformed microstructure similar to Fig. 7(b) with the occurrence of detwinning. Figs. 7(d) and 8(d) show the TEM images of V0.7 micro-pillar after compression test. A diffused ring of amorphous phase and fcc patterns were identified in Fig. 8(d). As Figs. 7(e) and 8(e) show, the V1.1 micro-pillar remains amorphous after compression, whereas no phase transformation was observed from SAED patterns after compression (Figs. 7 and 8) compared with Fig. 2. Using the in situ TEM observation of nano-indentation of nanotwinned Cu films and atomistic simulations, annihilation of twin boundaries was confirmed and detwinning only reverted thin twins into matrix crystals, which did not significantly increase the average thickness of twins [70]. In addition, as the energies of twin boundaries are one order of magnitude lower than that of grain boundaries, the twin boundaries are thought to be more stable against migration than grain boundaries during deformation [70]. It is inferred that, during deformation, nanotwins in CoCrFeMnNiV_x HEAFs are unstable and the detwinning behavior dominantly contribute to strain hardening.

4. Conclusions

In the present work, homogenous CoCrFeMnNiV_x ($x=0, 0.07, 0.3, 0.7, \text{ and } 1.1$) HEAFs were fabricated by magnetron co-sputtering and the effects of V addition on their microstructures associated with the corresponding mechanical properties were systematically studied. While CoCrFeMnNi HEAF presented a single fcc solid solution, films with V addition less than 6.0 at.% (i.e., $x < 0.3$) maintained the fcc structure. Co-sputtering with an excessive V would result in the formation of amorphous phase when $x \geq 0.3$. Each element distributed uniformly in all as-deposited

films. Meanwhile, a notable amount of nanotwins were found in V0, V0.07 and V0.3 films. Microhardness and micro-pillar compression tests demonstrated that the addition of V less than 6.0 at.% made a contribution to ultrahigh hardness and yield strength with little strength-ductility trade-off. However, nanotwins were unstable during deformation and the occurrence of detwinning would result in strain hardening. Although excessive V concentration is pronounced to restrain crystallization as well as the compressive strain, all CoCrFeMnNiV_x HEAFs exhibited the better mechanical properties in contrast with their bulk counterparts^[28]. Therefore, magnetron sputtering with the high-energy bombardment of atoms and faster quenching is an effective process to enhance the mechanical properties of HEAFs by generating nanotwins in nanograins.

Author contribution

Shuang Fang: Conceptualization, Methodology, Writing - original draft. Cheng Wang: Validation, Investigation, Writing - review & editing. Chia-Lin Li: Investigation. Jun-Hua Luan: Investigation. Zeng-Bao Jiao: Investigation. Chain-Tsuan Liu: Supervision. Chun-Hway Hsueh: Conceptualization, Supervision, Writing - review & editing, Funding acquisition.

Declaration of competing interest

None.

Acknowledgements

The work was supported by the Ministry of Science and Technology, Taiwan under Contract No. MOST 108-2218-E-002-062.

References

1. J.W. Yeh, S.K. Chen, S.J. Lin, J.Y. Gan, T.S. Chin, T.T. Shun, C.H. Tsau, S.Y. Chang, Nanostructured high-entropy alloys with multiple principal elements: novel alloy design concepts and outcomes, *Adv. Eng. Mater.* 6 (2004) 299.
2. B. Cantor, I. Chang, P. Knight, A. Vincent, Microstructural development in equiatomic multicomponent alloys, *Mater. Sci. Eng. A Struct.* 375 (2004) 213.
3. C.C. Tung, J.W. Yeh, T.T. Shun, S.K. Chen, Y.S. Huang, H.C. Chen, On the elemental effect of AlCoCrCuFeNi high-entropy alloy system, *Mater. Lett.* 61 (2007) 1.
4. K. Zhang, Z. Fu, J. Zhang, W. Wang, H. Wang, Y. Wang, Q. Zhang, J. Shi, Microstructure and mechanical properties of CoCrFeNiTiAl_x high-entropy alloys, *Mater. Sci. Eng. A Struct.* 508 (2009) 214.
5. W.R. Wang, W.L. Wang, S.C. Wang, Y.C. Tsai, C.H. Lai, J.W. Yeh, Effects of Al addition on the microstructure and mechanical property of Al_xCoCrFeNi high-entropy alloys, *Intermetallics* 26 (2012) 44.
6. J. He, W. Liu, H. Wang, Y. Wu, X. Liu, T. Nieh, Z. Lu, Effects of Al addition on structural evolution and tensile properties of the FeCoNiCrMn high-entropy alloy system, *Acta Mater.* 62 (2014) 105.
7. Z. Fu, W. Chen, H. Wen, D. Zhang, Z. Chen, B. Zheng, Y. Zhou, E.J. Lavernia, Microstructure and strengthening mechanisms in an FCC structured single-phase nanocrystalline Co₂₅Ni₂₅Fe₂₅Al_{7.5}Cu_{17.5} high-entropy alloy, *Acta Mater.* 107 (2016) 59.
8. Y. Zhang, T.T. Zuo, Z. Tang, M.C. Gao, K.A. Dahmen, P.K. Liaw, Z.P. Lu, Microstructures and properties of high-entropy alloys, *Prog. Mater. Sci.* 61 (2014) 1.
9. C. Li, J. Li, M. Zhao, Q. Jiang, Effect of alloying elements on microstructure and properties of multiprincipal elements high-entropy alloys, *J. Alloy. Comp.* 475 (2009) 752.

10. J. Pan, T. Dai, T. Lu, X. Ni, J. Dai, M. Li, Microstructure and mechanical properties of Nb₂₅Mo₂₅Ta₂₅W₂₅ and Ti₈Nb₂₃Mo₂₃Ta₂₃W₂₃ high entropy alloys prepared by mechanical alloying and spark plasma sintering, *Mater. Sci. Eng. A Struct.* 738 (2018) 362.
11. Z. Lei, X. Liu, Y. Wu, H. Wang, S. Jiang, S. Wang, X. Hui, Y. Wu, B. Gault, P. Kontis, Enhanced strength and ductility in a high-entropy alloy via ordered oxygen complexes, *Nature* 563 (2018) 546.
12. D. Li, C. Li, T. Feng, Y. Zhang, G. Sha, J.J. Lewandowski, P.K. Liaw, Y. Zhang, High-entropy Al_{0.3}CoCrFeNi alloy fibers with high tensile strength and ductility at ambient and cryogenic temperatures, *Acta Mater.* 123 (2017) 285.
13. H. Cheng, X. Liu, Q. Tang, W. Wang, X. Yan, P. Dai, Microstructure and mechanical properties of FeCoCrNiMnAl_x high-entropy alloys prepared by mechanical alloying and hot-pressed sintering, *J. Alloy. Comp.* 775 (2019) 742.
14. N. Stepanov, D. Shaysultanov, R. Chernichenko, N.Y. Yurchenko, S. Zhrebtsov, M. Tikhonovsky, G. Salishchev, Effect of thermomechanical processing on microstructure and mechanical properties of the carbon-containing CoCrFe-NiMn high entropy alloy, *J. Alloy. Comp.* 693 (2017) 394.
15. B. Gwalani, A.V. Ayyagari, D. Choudhuri, T. Scharf, S. Mukherjee, M. Gibson, R. Banerjee, Microstructure and wear resistance of an intermetallic-based Al_{0.25}Ti_{0.75}CoCrFeNi high entropy alloy, *Mater. Chem. Phys.* 210 (2018) 197.
16. M.H. Chuang, M.H. Tsai, W.R. Wang, S.J. Lin, J.W. Yeh, Microstructure and wear behavior of Al_xCo_{1.5}CrFeNi_{1.5}Ti_y high-entropy alloys, *Acta Mater.* 59 (2011) 6308.
17. O. Senkov, S. Senkova, D. Dimiduk, C. Woodward, D. Miracle, Oxidation behavior of a refractory NbCrMo_{0.5}Ta_{0.5}TiZr alloy, *J. Mater. Sci.* 47 (2012) 6522.

18. M.G. Poletti, G. Fiore, F. Gili, D. Mangherini, L. Battezzati, Development of a new high entropy alloy for wear resistance: FeCoCrNiW_{0.3} and FeCoCrNiW_{0.3+5} at.% of C, Mater. Des. 115 (2017) 247.
19. Y. Lu, H. Huang, X. Gao, C. Ren, J. Gao, H. Zhang, S. Zheng, Q. Jin, Y. Zhao, C. Lu, T. Wang, T. Li, A promising new class of irradiation tolerant materials: Ti₂ZrHfV_{0.5}Mo_{0.2} high-entropy alloy, J. Mater. Sci. Technol. 35 (2019) 369.
20. Y. Lu, Y. Dong, S. Guo, L. Jiang, H. Kang, T. Wang, B. Wen, Z. Wang, J. Jie, Z. Cao, A promising new class of high-temperature alloys: eutectic high-entropy alloys, Sci. Rep. 4 (2014) 6200.
21. Y. Lu, X. Gao, L. Jiang, Z. Chen, T. Wang, J. Jie, H. Kang, Y. Zhang, S. Guo, H. Ruan, Directly cast bulk eutectic and near-eutectic high entropy alloys with balanced strength and ductility in a wide temperature range, Acta Mater. 124 (2017) 143.
22. X. Feng, J. Zhang, K. Wu, X. Liang, G. Liu, J. Sun, Ultrastrong Al_{0.1}CoCrFeNi high-entropy alloys at small scales: effects of stacking faults vs. nanotwins, Nanoscale 10 (2018) 13329.
23. B. Gludovatz, A. Hohenwarter, D. Catoor, E.H. Chang, E.P. George, R.O. Ritchie, A fracture-resistant high-entropy alloy for cryogenic applications, Science 345 (2014) 1153.
24. F. Otto, A. Dlouhý, C. Somsen, H. Bei, G. Eggeler, E.P. George, The influences of temperature and microstructure on the tensile properties of a CoCrFeMnNi high-entropy alloy, Acta Mater. 61 (2013) 5743.
25. S. Zherebtsov, N. Stepanov, Y. Ivanisenko, D. Shaysultanov, N. Yurchenko, M. Klimova, G. Salishchev, Evolution of microstructure and mechanical properties of a CoCrFeMnNi high-entropy alloy during high-pressure torsion at room and cryogenic temperatures, Metals 8 (2018) 123.

26. G. Salishchev, M. Tikhonovsky, D. Shaysultanov, N. Stepanov, A. Kuznetsov, I. Kolodiy, A. Tortika, O. Senkov, Effect of Mn and V on structure and mechanical properties of high-entropy alloys based on CoCrFeNi system, *J. Alloy. Comp.* 591 (2014) 11.
27. A. Gali, E.P. George, Tensile properties of high-and medium-entropy alloys, *Intermetallics* 39 (2013) 74.
28. N. Stepanov, D. Shaysultanov, G. Salishchev, M. Tikhonovsky, E. Oleynik, A. Tortika, O. Senkov, Effect of V content on microstructure and mechanical properties of the CoCrFeMnNiV_x high entropy alloys, *J. Alloy. Comp.* 628 (2015) 170.
29. E. Tabachnikova, A. Podolskiy, M. Laktionova, N. Bereznaia, M. Tikhonovsky, A. Tortika, Mechanical properties of the CoCrFeNiMnV_x high entropy alloys in temperature range 4.2-300 K, *J. Alloy. Compd.* 698 (2017) 501.
30. D. Shaysultanov, N. Stepanov, G. Salishchev, M. Tikhonovsky, Effect of heat treatment on the structure and hardness of high-entropy alloys CoCrFe-NiMnV_x (x=0.25, 0.5, 0.75, 1), *Phys. Met. Metallogr.* 118 (2017) 579.
31. S. Niu, H. Kou, Y. Zhang, J. Wang, J. Li, The characteristics of serration in Al_{0.5}CoCrFeNi high entropy alloy, *Mater. Sci. Eng. A Struct.* 702 (2017) 96.
32. J. Brechtel, S. Chen, X. Xie, Y. Ren, J. Qiao, P. Liaw, S. Zinkle, Towards a greater understanding of serrated flows in an Al-containing high-entropy-based alloy, *Int. J. Plast.* 115 (2019) 71.
33. G. Qin, R. Chen, H. Zheng, H. Fang, L. Wang, Y. Su, J. Guo, H. Fu, Strengthening FCC-CoCrFeMnNi high entropy alloys by Mo addition, *J. Mater. Sci. Technol.* 35 (2019) 578.

34. C. Wang, T.H. Li, Y.C. Liao, C.L. Li, J.S.C. Jang, C.H. Hsueh, Hardness and strength enhancements of CoCrFeMnNi high-entropy alloy with Nd doping, *Mater. Sci. Eng. A Struct.* (2019) 138192.
35. J. Chen, Z. Yao, X. Wang, Y. Lu, X. Wang, Y. Liu, X. Fan, Effect of C content on microstructure and tensile properties of as-cast CoCrFeMnNi high entropy alloy, *Mater. Chem. Phys.* 210 (2018) 136.
36. H. Shahmir, M. Nili Ahmadabadi, A. Shafiee, M. Andrzejczuk, M. Lewandowska, T.G. Langdon, Effect of Ti on phase stability and strengthening mechanisms of a nanocrystalline CoCrFeMnNi high-entropy alloy, *Mater. Sci. Eng. A Struct.* 725 (2018) 196.
37. H. Cheng, W. Chen, X. Liu, Q. Tang, Y. Xie, P. Dai, Effect of Ti and C additions on the microstructure and mechanical properties of the FeCoCrNiMn high-entropy alloy, *Mater. Sci. Eng. A Struct.* 719 (2018) 192.
38. Y. Dong, K. Zhou, Y. Lu, X. Gao, T. Wang, T. Li, Effect of vanadium addition on the microstructure and properties of AlCoCrFeNi high entropy alloy, *Mater. Des.* 57 (2014) 67.
39. E. Tabachnikova, A. Podolskiy, M. Laktionova, N. Bereznaiia, M. Tikhonovsky, A. Tortika, Mechanical properties of the CoCrFeNiMnV_x high entropy alloys in temperature range 4.2-300 K, *J. Alloy. Compd.* 698 (2017) 501.
40. W. Li, P. Liu, P.K. Liaw, Microstructures and properties of high-entropy alloy films and coatings: a review, *Mater. Res. Lett.* 6 (2018) 199.
41. L. Liu, J. Zhu, C. Hou, J. Li, Q. Jiang, Dense and smooth amorphous films of multicomponent FeCoNiCuVZrAl high-entropy alloy deposited by direct current magnetron sputtering, *Mater. Des.* 46 (2013) 675.

42. W. Huo, X. Liu, S. Tan, F. Fang, Z. Xie, J. Shang, J. Jiang, Ultrahigh hardness and high electrical resistivity in nano-twinned, nanocrystalline high-entropy alloy films, *Appl. Surf. Sci.* 439 (2018) 222.
43. B. Braeckman, F. Boydens, H. Hidalgo, P. Dutheil, M. Jullien, A.L. Thomann, D. Depla, High entropy alloy thin films deposited by magnetron sputtering of powder targets, *Thin Solid Films* 580 (2015) 71.
44. T.K. Chen, M.S. Wong, T.T. Shun, J.W. Yeh, Nanostructured nitride films of multi-element high-entropy alloys by reactive DC sputtering, *Surf. Coat. Technol.* 200 (2005) 1361.
45. W. Liao, S. Lan, L. Gao, H. Zhang, S. Xu, J. Song, X. Wang, Y. Lu, Nanocrystalline high-entropy alloy (CoCrFeNiAl_{0.3}) thin-film coating by magnetron sputtering, *Thin Solid Films* 638 (2017) 383.
46. X. Li, Z. Zheng, D. Dou, J. Li, Microstructure and properties of coating of FeAlCuCrCoMn high entropy alloy deposited by direct current magnetron sputtering, *Mater. Res.* 19 (4) (2016) 802-806.
47. Z. An, H. Jia, Y. Wu, P.D. Rack, A.D. Patchen, Y. Liu, Y. Ren, N. Li, P.K. Liaw, Solid-solution CrCoCuFeNi high-entropy alloy thin films synthesized by sputter deposition, *Mater. Res. Lett.* 3 (4) (2015) 203-209.
48. Y. Zou, H. Ma, R. Spolenak, Ultrastrong ductile and stable high-entropy alloys at small scales, *Nat. Commun.* 6 (2015) 7748.
49. X. Feng, W. Fu, J. Zhang, J. Zhao, J. Li, K. Wu, G. Liu, J. Sun, Effects of nanotwins on the mechanical properties of Al_xCoCrFeNi high entropy alloy thin films, *Scr. Mater.* 139 (2017) 71.

50. B. Braeckman, F. Misják, G. Radnóczy, M. Caplovicová, P. Djemia, F. Tétard, L. Belliard, D. Depla, The nanostructure and mechanical properties of nano- composite Nb_x-CoCrCuFeNi thin films, *Scr. Mater.* 139 (2017) 155.
51. B. Braeckman, D. Depla, Structure formation and properties of sputter deposited Nb_x-CoCrCuFeNi high entropy alloy thin films, *J. Alloy. Comp.* 646 (2015) 810.
52. P. Bhattacharjee, G. Sathiaraj, M. Zaid, J. Gatti, C. Lee, C.W. Tsai, J.W. Yeh, Microstructure and texture evolution during annealing of equiatomic CoCr- FeMnNi high-entropy alloy, *J. Alloy. Comp.* 587 (2014) 544.
53. J.A. Thornton, D. Hoffman, Stress-related effects in thin films, *Thin Solid Films* 171 (1) (1989) 5.
54. Y. Zhang, Y.J. Zhou, J.P. Lin, G.L. Chen, P.K. Liaw, Solid-solution phase formation rules for multi-component alloys, *Adv. Eng. Mater.* 10 (2008) 534.
55. X. Yang, Y. Zhang, Prediction of high-entropy stabilized solid-solution in multi-component alloys, *Mater. Chem. Phys.* 132 (2012) 233.
56. R. Qu, Z. Liu, G. Wang, Z. Zhang, Progressive shear band propagation in metallic glasses under compression, *Acta Mater.* 91 (2015) 19.
57. A. Greer, Y. Cheng, E. Ma, Shear bands in metallic glasses, *Mater. Sci. Eng. R Rep.* 74 (4) (2013) 71-132.
58. C.S. Chen, P. Yiu, C.L. Li, J.P. Chu, C.H. Shek, C.H. Hsueh, Effects of annealing on mechanical behavior of Zr-Ti-Ni thin film metallic glasses, *Mater. Sci. Eng. A Struct.* 608 (2014) 258.

59. Y.H. Wu, C. Wang, C.H. Hsueh, T.H. Li, C.H. Chang, H.C. Chen, J.S.C. Jang, J.C. Huang, Z.H. Ma, Microstructure and mechanical properties of Zr-Ti-Cu-Nd metallic glass composites, *J. Alloy. Comp.* 702 (2017) 318.
60. A. Zaddach, C. Niu, C. Koch, D. Irving, Mechanical properties and stacking fault energies of NiFeCrCoMn high-entropy alloy, *JOM* 65 (2013) 1780.
61. M.C. Gao, C. Niu, C. Jiang, D.L. Irving, Applications of Special Quasi-Random Structures to High-Entropy Alloys, *High-Entropy Alloys*, Springer, 2016, p. 333.
62. O. Bouaziz, S. Allain, C. Scott, Effect of grain and twin boundaries on the hardening mechanisms of twinning-induced plasticity steels, *Scr. Mater.* 58 (2008) 484.
63. I. Gutierrez-Urrutia, D. Raabe, Grain size effect on strain hardening in twinning-induced plasticity steels, *Scr. Mater.* 66 (2012) 992.
64. Z. Li, K.G. Pradeep, Y. Deng, D. Raabe, C.C. Tasan, Metastable high-entropy dual-phase alloys overcome the strength-ductility trade-off, *Nature* 534 (2016) 227.
65. S. Sun, Y. Tian, H. Lin, H. Yang, X. Dong, Y. Wang, Z. Zhang, Transition of twinning behavior in CoCrFeMnNi high entropy alloy with grain refinement, *Mater. Sci. Eng. A Struct.* 712 (2018) 603.
66. L. Lu, X. Chen, X. Huang, K. Lu, Revealing the maximum strength in nano-twinned copper, *Science* 323 (2009) 607.
67. D.A. Porter, K.E. Easterling, M. Sherif, *Phase Transformations in Metals and Alloys*, CRC Press, 2009.
68. J.Y. Kim, D. Jang, J.R. Greer, Tensile and compressive behavior of tungsten, molybdenum, tantalum and niobium at the nanoscale, *Acta Mater.* 58 (2010) 2355.

69. Y. Deng, C.C. Tasan, K.G. Pradeep, H. Springer, A. Kostka, D. Raabe, Design of a twinning-induced plasticity high entropy alloy, *Acta Mater.* 94 (2015) 124.
70. J. Wang, N. Li, O. Anderoglu, X. Zhang, A. Misra, J.Y. Huang, J.P. Hirth, Detwinning mechanisms for growth twins in face-centered cubic metals, *Acta Mater.* 58 (2010) 2262.

Figure captions

Fig. 1. XRD patterns of CoCrFeMnNiV_x (x = 0, 0.07, 0.3, 0.7, and 1.1) HEAFs.

Fig. 2. TEM images of CoCrFeMnNiV_x (x = 0, 0.07, 0.3, 0.7, and 1.1) HEAFs with the inset showing the corresponding SAED patterns for (a) V0, (b) V0.07, (c) V0.3 and (d) V0.7. (e) The HRTEM image of V1.1 with the SAED pattern shown in the inset.

Fig. 3. 3D APT element distribution reconstruction of (a) CoCrFeMnNi and (b) CoCrFeMnNiV_{0.07} HEAFs.

Fig. 4. SEM images of as-compressed CoCrFeMnNiV_x HEAFs for (a) V0, (b) V0.07, (c) V0.3, (d) V0.7, and (e) V1.1.

Fig. 5. Engineering compressive stress-strain curves of CoCrFeMnNiV_x HEAFs. Curves are offset horizontally from the origin for clear viewing.

Fig. 6. Hardness and Young's modulus of CoCrFeMnNiV_x HEAFs as functions of the power applied on the V target.

Fig. 7. TEM images of CoCrFeMnNiV_x HEAFs after micro-pillar compression tests for (a) V0, (b) V0.07, (c) V0.3, (d) V0.7 and (e) V1.1.

Fig. 8. Magnified images of the deformed zones in CoCrFeMnNiV_x HEAFs after micro-pillar compression tests for (a) V0, (b) V0.07, (c) V0.3, (d) V0.7 and (e) V1.1. The corresponding SAED pattern is shown in inset.

Fig. 1

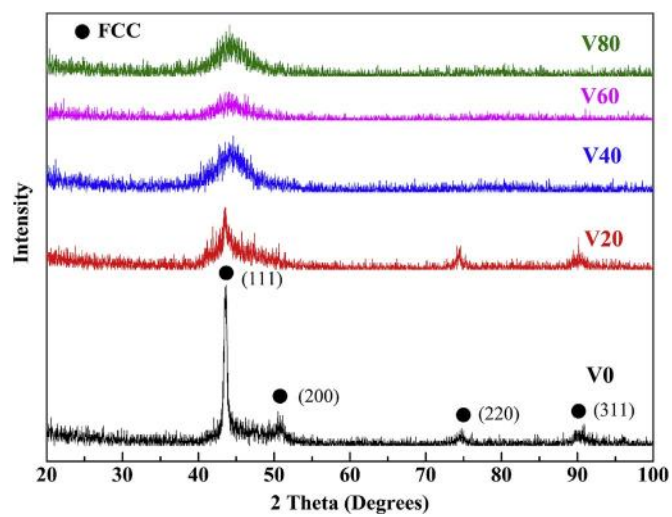


Fig. 2

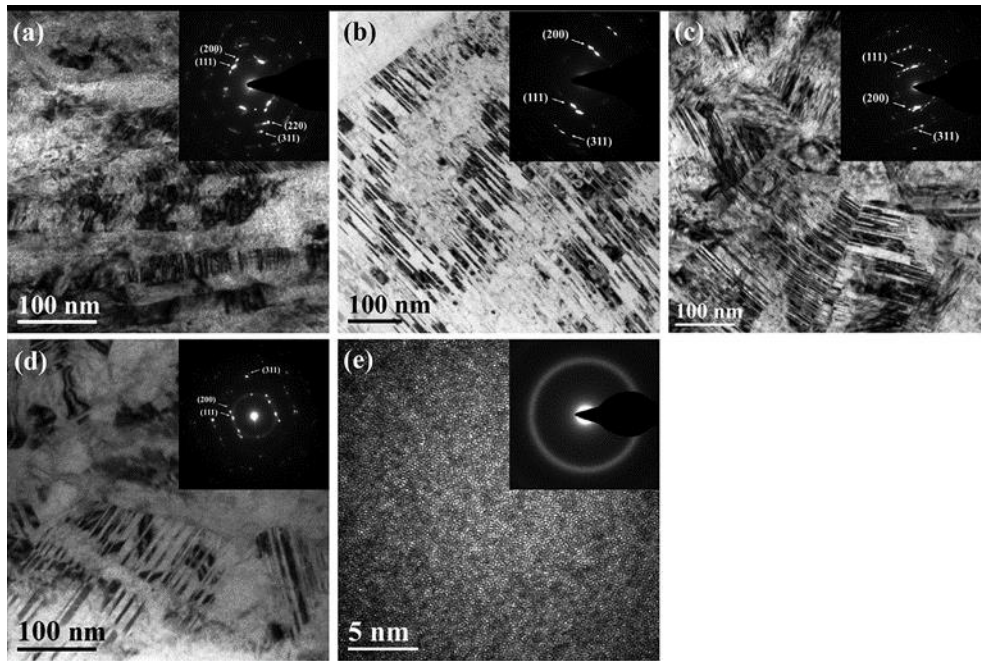


Fig. 3

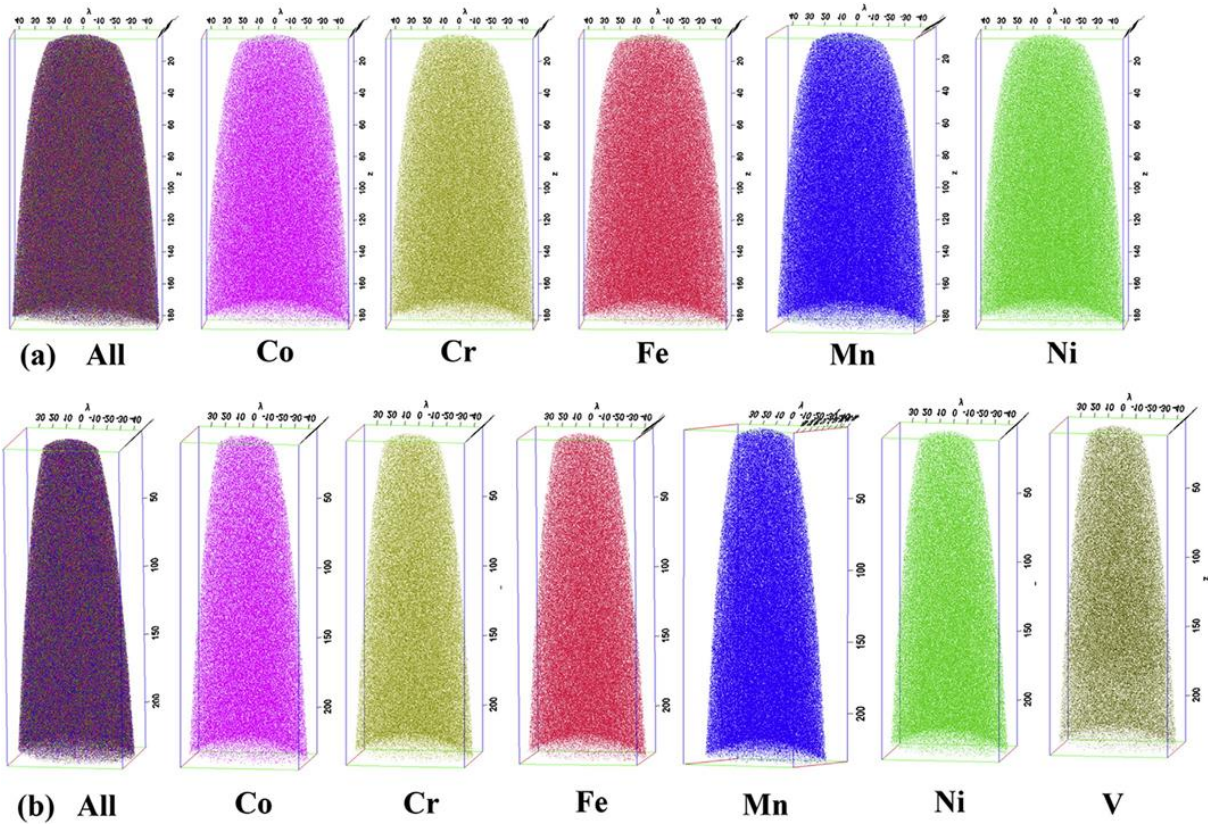


Fig. 4

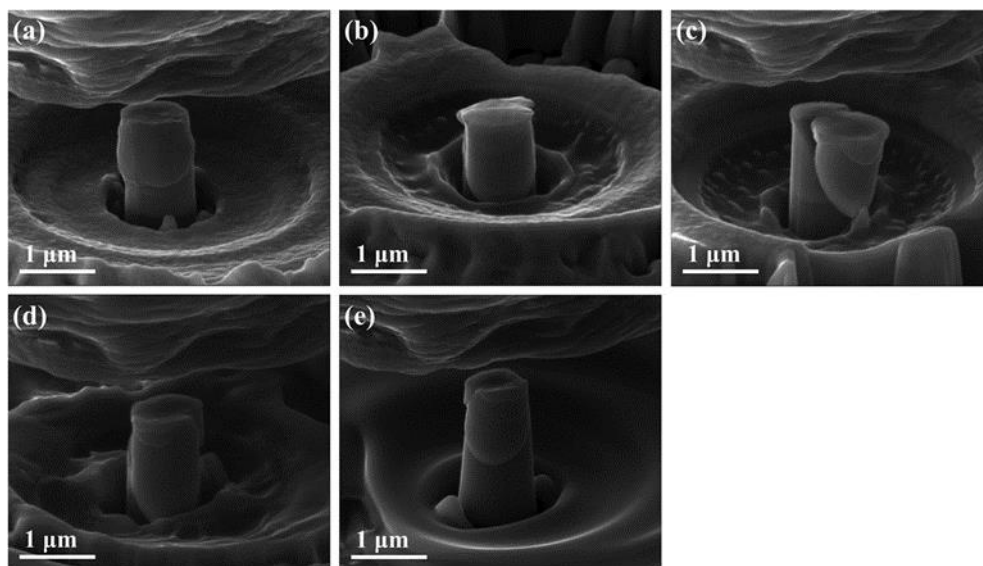


Fig. 5

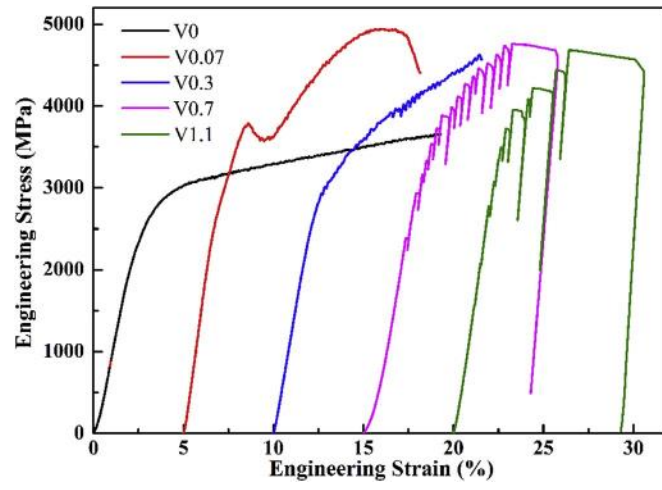


Fig. 6

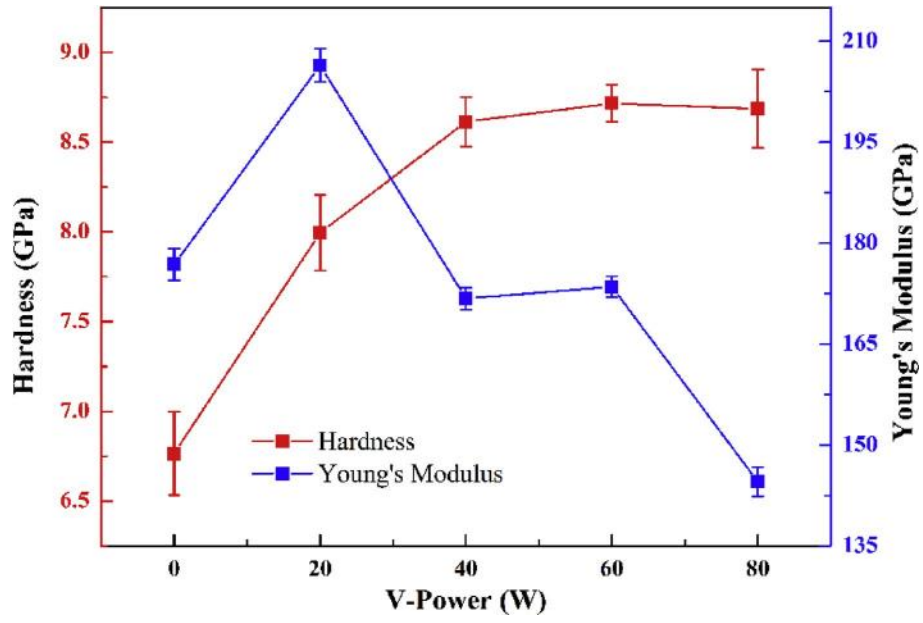


Fig. 7

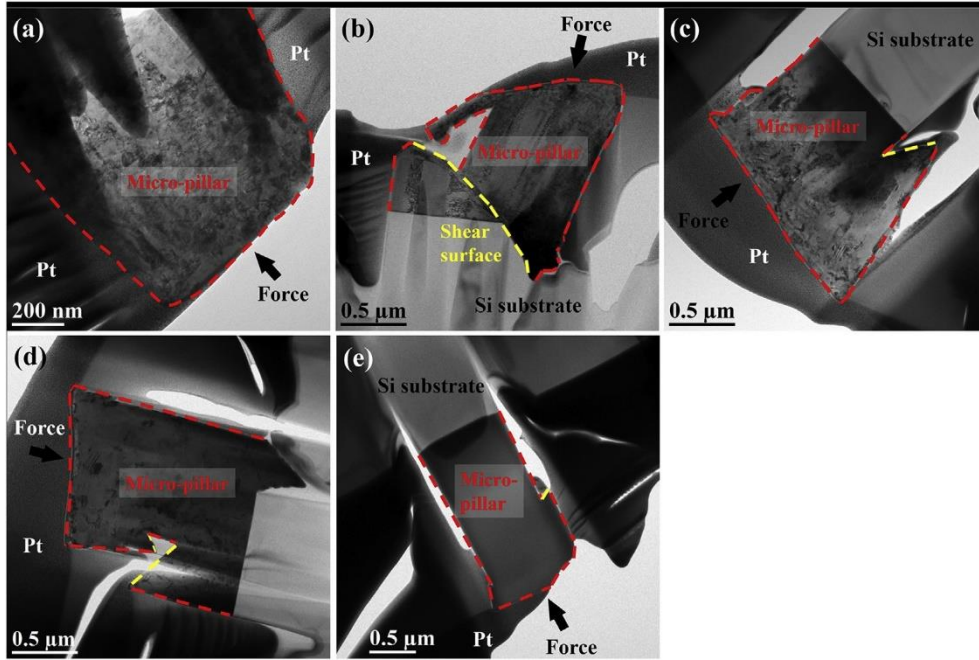


Fig. 8

